A Back Propagation Neural Network-Based Radiometric Correction Method (BPNNRCM) for UAV Multispectral Image

Yin Zhang, Qingwu Hu, Hailong Li, Jiayuan Li, Tiancheng Liu, Yuting Chen, Mingyao Ai, and Jianye Dong

***Abstract*—Radiometric correction is one of the most important preprocessing parts of unmanned aerial vehicle (UAV) multispectral remote sensing data analysis and application. In this article, a back propagation (BP) neural network-based radiometric correction method (BPNNRCM) considering optimal parameters was proposed. First, we used different UAV multispectral sensors (K6 equipped on the DJI M600, D-MSPC2000 equipped on the FEIMA D2000) to collect training, validation, testing and cross-validation data. Second, the radiometric correction results of BP neural network with different input variables and hidden layer node number were compared to select the best combination of input parameters and hidden layer node number. Finally, the radiometric correction accuracy and robustness of BP neural network considering the optimal parameters were verified. When the number of nodes in the input layer was five (digital number, UAV sensor height, wavelength, solar altitude angle, and temperature) and the number of nodes in the hidden layer was eight, the BP neural network had the best comprehensive performance in training time of train set and accuracy of validation/test set. In the aspect of accuracy and robustness, the absolute errors of test and cross-validation images' surface reflectance obtained by the BPNNRCM were all less than 0.054. The BPNNRCM had smaller average absolute error (0.0141), mean squared error (0.0003), mean absolute error (0.0141) and mean relative error (7.1%) comparing with empirical line method and radiative transfer model. In general, the research results of this article prove the feasibility and prospect of BPNNRCM for radiometric correction of UAV multispectral images.**

***Index Terms*—Back propagation (BP) neural network, optimal parameters, radiometric correction, surface reflectance (SR), unmanned aerial vehicle (UAV) remote sensing.**

I. Introduction

With the development of the unmanned aerial vehicle (UAV) platform and sensor technology, UAV remote sensing has achieved rapid development. Compared with traditional aviation and aerospace remote sensing image acquisition methods, UAV as a data acquisition platform has many advantages such as low cost, flexible takeoff and landing, fast and efficiency, intuitive and comprehensive, and low flight altitude. UAV remote sensing is an important supplementary approach to satellite remote sensing. The image data obtained by multispectral/hyperspectral sensors mounted on UAV can provide effective quantitative inversion and interpretation data basis for resource exploration, camouflage survey, agricultural monitoring and many other directions, and has a wide application prospect in many fields [1], [2], [3], [4], [5], [6], [7], [8].

Due to its low cost and readily available data, UAV remote sensing is now widely used to obtain various surface biological, physical and chemical parameters in specified areas. Therefore, it is very important to accurately retrieve the surface reflectance (SR) from UAV remote sensing data before quantitative analysis. Radiometric correction [converting the digital numbers (DN value) received by UAV sensor into the SR] is an important and key research problem in the application of UAV images in many fields. In the process of UAV sensor imaging, even if the flight altitude is low, the radiation signal of the target object will be scattered and absorbed by different types of atmospheric components during transmission in the atmosphere, and the radiation signal received by the sensor will produce interference and distortion to a certain extent. Therefore, radiometric correction is a necessary part in the article of quantification and refinement of UAV multispectral images.

According to different principles, radiometric correction methods can be divided into relative correction method based on image feature, the empirical line method (ELM) [9], [10], [11], [12], [13], [14], [15], the method for measuring the incident radiation using spectroradiometer and camera irradiance sensor during flying [16], [17], [18], [19], and method based on atmospheric radiative transfer model. Image-based radiometric correction methods mainly include histogram matching method [20], [21], invariant target method [22], [23], dark pixel method [24], [25], [26], T–C transform [27], haze optimized transform [28]. Although ELM method is intuitive and easy to implement, the quality and accuracy of SR products based on ELM method will be greatly reduced if the number of ground calibration targets is small or they do not have Lambertian properties [29], [30], [31]. After decades of development of spectral imaging

Manuscript received 5 May 2022; revised 5 July 2022; accepted 11 November 2022. Date of publication 21 November 2022; date of current version 7 December 2022. This work was supported in part by the National Key R&D Program of China under Grant 2021YFB2600401, and in part by the Stable-Support Scientific Project of China Research Institute of Radiowave Propagation under Grant A131903W07. *(Corresponding author: Qingwu Hu.)*

Yin Zhang, Qingwu Hu, Jiayuan Li, Tiancheng Liu, Yuting Chen, and Mingyao Ai are with the School of Remote Sensing and Information Engineering, Wuhan University, Wuhan 430079, China (e-mail: 2020202130084@whu.edu.cn; huqw@whu.edu.cn; ljy_whu_2012@whu.edu.cn; 2018302130035@whu.edu.cn; yt.chen@whu.edu.cn; aimingyao@whu.edu.cn).

Hailong Li and Jianye Dong are with the China Research Institute of Radiowave Propagation, Xinxiang 453003, China (e-mail: lufeilong1991@163.com; dongjy@crirp.ac.cn).

Digital Object Identifier 10.1109/JSTARS.2022.3223781

technology, the theory and model of electromagnetic wave transmission have been relatively mature. The representative mature radiative transfer models [32], [33], [34] include (second simulation of the satellite signal in the solar spectrum (6S), LOW resolution TRANsmission model), MODerate resolution TRANsmission model (MODTRAN). Many scholars have used different models to study and apply radiometric correction to remote sensing data of different scenarios and types [35], [36], [37], [38], [39], [40], [41]. Based on rigorous mathematical and physical theories, the radiative transfer model scientifically presents the transmission process of electromagnetic radiation in the "sun-earth-sensor" system, which has definite physical significance. The MODTRAN and 6S models have been proved to have high accuracy by many previous studies [42], [43], [44], [45], [46], [47]. However, there is an important prerequisite for applying 6S and MODTRAN models: depend on accurate parameter information about aerosol and atmosphere. In addition, due to the complexity of atmospheric influence on electromagnetic waves and the complexity of solving radiative transfer equation (6S, MODTRAN and other radiative transfer models use different methods to approximate solving the equation), there must be some errors in the calculation results of MODTRAN and 6S models.

The main objective of this article is to propose a user-friendly and robust radiometric correction method that requires less and easily accessible input parameters. In this article, we propose a radiometric correction algorithm based on back propagation (BP) neural network with optimal parameters to obtain the UAV multispectral SR products. We dub our algorithm back propagation neural network-based radiometric correction method (BPNNRCM). Experimental results show that BPNNRCM can effectively avoid the complex mathematical and physical process of atmospheric radiative transfer and the change of atmospheric physical and chemical parameters. The BPNNRCM has high self-learning and self-adaptive ability, can perform radiometric correction for images of multispectral bands, and can calculate the reflectance with high precision under the common flight conditions of UAV.

II. Materials and Methods

The research route of this article is displayed in Fig. 1. Our study can be divided into four parts. First, we collected training dataset, validation dataset, test dataset, and cross-validation dataset under different environmental conditions (see Section II-A). Second, the optimal parameters (different input parameters and different numbers of hidden layer nodes) of BP neural network for radiometric correction were selected [see Section II-B-d and Section III-A]. Besides, the accuracy of the radiometric correction model based on BP neural network with optimal parameters was evaluated (see Section III-B). Finally, based on cross-validation, the robustness and generalization of the radiometric correction method proposed in this article (BPNNRCM) were assessed (see Section III-C).

A. Data

The UAV multispectral data (DJI Matrice 600 [see Fig. 2(a)]: https://www.dji.com/cz/matrice600; Sensor [see Fig. 2(b)]: K6 airborne multispectral imager, http://azup.com.cn/newsinfo/1163647.html) were collected in the brick land (Location: 113.506384872°E, 30.948106339°N; Date: June 5, 2021) and grassland (Location: 113.506418036°E, 30.978097257°N; Date: June 6, 2021) in Yingcheng National Mine Park, Hubei Province of China. Reflective boards with reflectance of 5%, 10%, 20%, 30%, 50%, 60%, and 70% were placed in the experimental site. In order to ensure the applicability and generalization ability of the BPNNRCM, the images of the above reflective boards with different heights (20 to 500 m, with intervals of 20 m), different times (10:00, 11:00, 11:30, 13:30, 15:30) and different bands (450, 550, 650, 725, and 850 nm) were included, and the corresponding real-time temperature data were recorded through the weather forecast app in the mobile phone (see Table I). Fig. 2(c) and (d) displays the spatial distribution of the reflective boards during the experiment. The length and width of all reflective boards in Fig. 2(c) and (d) are 1 m. Ground sampling distance (GSD) of UAV image increases with the increase of flight altitude. When the flight altitude of UAV is 500 m (the maximum flying altitude of DJI UAV when the ban is not lifted), the GSD of multispectral image obtained by K6 is 18 cm/pix. MAPIR camera control (MCC) is a Windows OS software package used to process images from K6 multispectral camera (https://www.mapir.camera/collections/software/products/mapir-camera-control). The maximum GSD

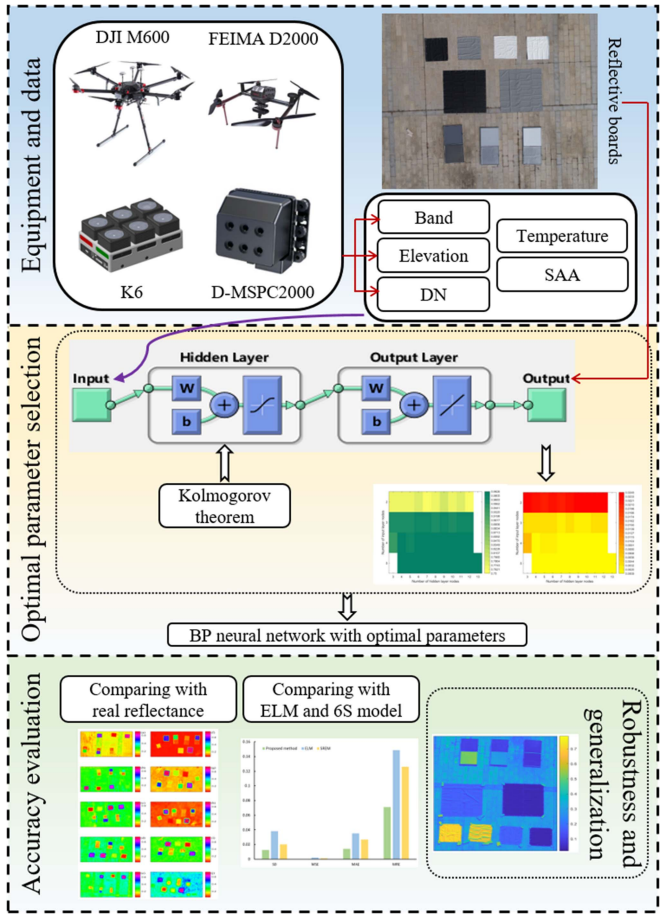

Fig. 1. Flowchart of the radiometric correction procedure.

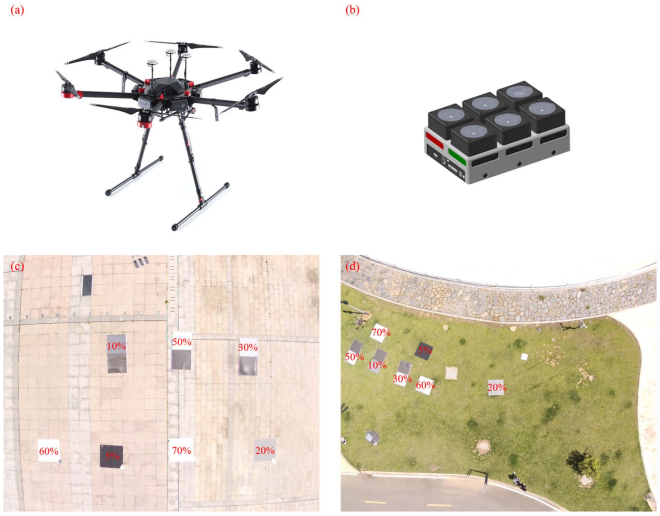

Fig. 2. Distribution of reflective boards in different experimental sites. (a) Unmanned aerial vehicle. (b) Sensor. (c) Brick land. (d) Grassland.

TABLE I
TEMPERATURE AND AQI DATA OF DIFFERENT EXPERIMENTAL SITES AT DIFFERENT TIMES

	Date	Site	Time	Temperature (°C)
Condition 1	2021.6.5	Brick	10:00	25
Condition 2	2021.6.5	Brick	11:00	27
Condition 3	2021.6.5	Brick	13:30	31
Condition 4	2021.6.5	Brick	15:30	30
Condition 5	2021.6.6	Grass	11:30	30
Condition 6	2021.6.6	Grass	13:30	33

of the UAV image we collected was 18 cm/pix, and the number of pixels occupied by the reflective boards was at least 25. We used MCC to convert the original multispectral data obtained by UAV into grid image (data format: TIFF), and then took the mean value of the three neighborhood in the center of the reflective board as its DN value on the multispectral image. The DN value was used as the input data for the training of neural network model.

FEIMA D2000 with D-MSPC2000 (http://www.feimarobotics.com/zhcn/productDetailD2000; https://www.163.com/dy/article/GEAL29VS05149OCK.html) was the UAV multispectral data acquisition equipment used for cross-validation (generalization validation of BPNNRCM). The multispectral sensor obtained images of six bands: 450; 555; 660; 720; 750; and 840 nm. UAV multispectral images were collected on December 14, 2021 in Yingcheng City, Hubei Province of China. The longitude and latitude of the experiment site were 113.496529°E and 30.946152°N, respectively. Reflectance of reflective boards with known reflectance were 5%, 10%, 20%, 30%, 50%, 60% and 70%, respectively. See Fig. 3(c) for the spatial distribution of the

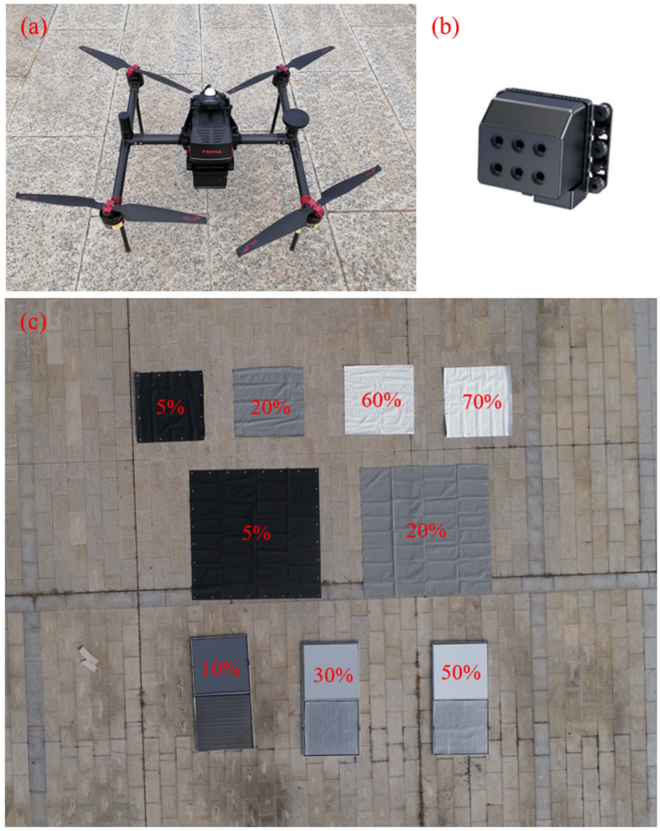

Fig. 3. (a) Unmanned aerial vehicle, (b) multispectral sensor, and (c) distribution of reflective boards.

TABLE II
UAV MULTISPECTRAL IMAGES TO VERIFY THE ROBUSTNESS AND GENERALIZATION OF BPNNRCM PROPOSED IN THIS ARTICLE

Image	Band (nm)	Image Height (m)	SAA (°)	Temperature (°C)
1	840	93	28.66	10
2	555	145	28.66	10

reflective boards. The sizes of the two large reflective boards (reflectance is 5% and 20%, respectively) in the second row are 2 m × 2 m, and the sizes of the other small reflective boards are 1 m × 1 m. In the process of images acquisition, solar altitude angle (SAA) and temperature was recorded synchronously. Table II gives the image information collected in this experiment. When the image height is 93 and 145 m, the GSD is 6.7 and 10.5 cm/pix, respectively. The temperature was recorded in the same way as mentioned above, that is, use the weather forecast app in the mobile phone to record the real-time temperature. FEIMA UAV Manager (FUM, http://www.feimarobotics.com/zhcn/productDetailManager) is an intelligent software system for UAV data acquisition, processing and display management. We used FUM to convert the original multispectral data obtained by FEIMA UAV into grid image (data format: TIFF), and then took the mean value of the three neighborhood in the center of the reflective board as its

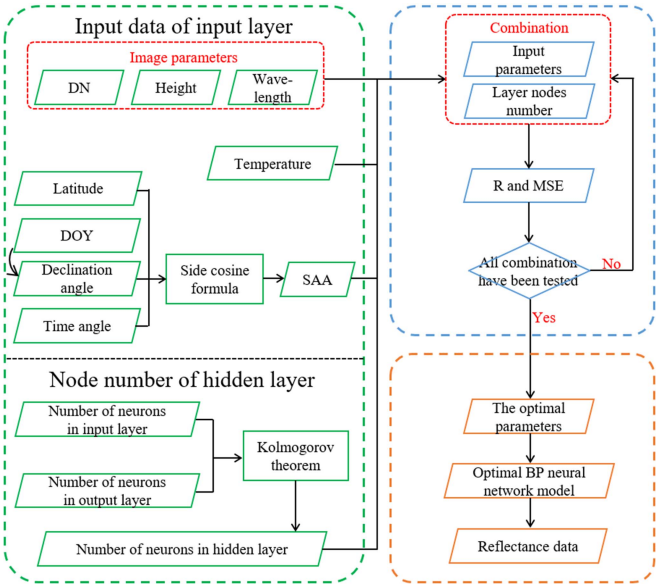

Fig. 4. Flow of UAV multispectral image radiometric correction based on BP neural network considering optimal parameters.

DN value on the multispectral image. The DN value was used as the input data for the training of neural network model. The reflectance of the reflective boards obtained by BPNNRCM was compared with the real reflectance of the reflective boards, so as to verify the generalization and robustness of the BPNNRCM.

B. Methods

The BPNNRCM, framework for UAV multispectral image radiometric correction based on BP neural network is shown in Fig. 4. UAV multispectral image parameters (DN value, image height and wavelength), climate factor (temperature) and SAA constituted the input parameters of BP neural network. According to the number of nodes in the input layer and output layer, combining with Kolmogorov theorem, the number of nodes in the hidden layer of BP neural network was obtained. Different input parameters and different hidden layer node numbers formed multiple combinations. According to the training time and accuracy of BP neural network model in the training and test dataset, the combination with the best effect (input parameters + hidden layers) was determined, and the corresponding radiometric correction model based on BP neural network was obtained, so as to achieve the transformation from DN value to SR of UAV multispectral image.

1) Back Propagation (BP) Neural Network: BP neural network is one of the most representative artificial neural network algorithms [48]. The topology structure of BP neural network model includes input layer, hidden layer, and output layer. The basic idea of BP neural network is to build a multilayer feedforward neural network, and adjust the connection weights and thresholds between each layer and each node by using the error between the actual output value and the expected output value of the signal value in the propagation process according to the error backward propagation algorithm. This algorithm does not need to determine the mathematical mapping between input and output in advance, but can use error feedback to learn rules and obtain mathematical simulation of the signal. The learning process of BP neural network is divided into two stages: the forward propagation process of input signal and the BP process of prediction error [49], [50].

Suppose there are m neurons in the output layer, and the actual output of BP neural network is y. The expected output is y'. The error (ε) of model is calculated as follows:

$$\varepsilon = \frac{1}{2}\sum_{j=1}^{m}(y_j - y'_j)^2. \tag{1}$$

The modified value of each weight value is

$$\Delta w_{ij} = -\eta\frac{\partial\varepsilon}{\partial\omega_{ij}} = -\eta\frac{\partial\varepsilon}{\partial I_j}\frac{\partial I_j}{\partial\omega_{ij}} \tag{2}$$

where w_{ij} is the weight from the input layer node i to the hidden layer node j. η represents the learning rate. I_j is the transfer function of the j_{th} hidden layer. There are many kinds of transfer functions of BP neural network, three of which are commonly used, namely Logsig, Tansig, and Purelin. The input value of Logsig, Tansig, and Purelin functions can take any value. The output value of the Logsig function is between 0 and 1, the output value of the Tansig function is between -1 and 1, and the output value of the Purelin function is arbitrary. Since SR of natural features is between 0 and 1, which is consistent with the output value range of Logsig-type function, Logsig is used as the transfer function of BP neural network in this article.

2) Number of Hidden Layer Nodes: Kolmogorov theorem can be used to determine the number of hidden layer nodes of BP neural network [51]

$$n_2 = \sqrt{n_1 + m + 1} + a \tag{3}$$

where n_2, n_1, and m represent the number of nodes in the hidden layer, input layer, and output layer respectively. The value of a is an integer ranging from 1 to 10.

3) Solar Altitude Angle: The SAA refers to the angle between the incident direction of sunlight and the ground plane at a certain place on the Earth. When the SAA angle is 90°, the solar radiation intensity is maximum. The change of SAA will affect the energy at the entrance pupil of UAV sensor. The SAA at a certain position at a certain time can be calculated by

$$\sin H = \sin\varphi\ \sin\delta + \cos\varphi\cos\delta\cos t \tag{4}$$

where H is the SAA, φ is the geographical latitude, δ is the solar declination of the day, and t represents the solar hour angle at that time. Solar declination is the angle between the Earth's equatorial plane and the line between the sun and the center of the Earth. The solar hour angle is the angle between the line of the sun's light hitting the Earth and the center of the Earth and the projection of the line of the sun at noon on the Earth's equatorial plane. Solar declination indicates the latitude of the point of direct exposure, with positive northern latitudes and negative southern latitudes. The calculation equation of solar declination angle on any date is

$$\sin\delta = 0.39795\cos\left[0.98563\,(N - 173)\right] \tag{5}$$

TABLE III
COMBINATIONS OF INPUT PARAMETERS AND HIDDEN LAYERS OF BP NEURAL NETWORK

	Input Data	Node Number of Input Layer	Node Number of Hidden Layer	Output Result
Combination 1	DN value Image height;	2	3 ~ 12	Surface reflectance
Combination 2	DN value Image height Wavelength;	3	3 ~ 12	Surface reflectance
Combination 3	DN value Image height Wavelength Solar altitude angle;	4	3 ~ 12	Surface reflectance
Combination 4	DN value Image height Wavelength Solar altitude angle Temperature	5	4 ~ 13	Surface reflectance

where N is the day of year, which is the serial number of the date in one year. For example, January 1 is 1, and December 31 in nonleap year is 365.

According to (4) and (5), the SAA of condition $1 \sim 6$ in Table I were 61.96°, 74.13°, 68.21°, 42.74°, 79.22°, and 68.25° respectively.

4) Input Parameter Combinations of BP Neural Network: In order to get the optimal parameters (input data and the number of hidden layer nodes) of BP neural network with the highest accuracy, we designed a variety of combinations of input data and hidden layer nodes number of BP neural network. This experiment was run on a PC (Windows 10 64-bit operating system) equipped with Intel i7-10700F CPU, 16G memory and NVIDIA GTX 1650 GPU. BP neural networks with different combinations of input data and hidden layer nodes number have the same epochs (500), learning rate (0.01), minimum gradient (1×10^{-7}) and global minimum error (1×10^{-5}). Table III gives all the combinations of input data, input layer node number and hidden layer node number of BP neural network model. The numbers of hidden layer nodes in Table III were obtained by (3). For example, when the input data of BP neural network model are DN value of reflective boards and image height (the height of the sensor above the ground), that is, the number of nodes in the input layer is 2, the number of nodes in the hidden layer is an integer between 3 and 12 calculated by (3). Therefore, combination 1 represents 10 different BP neural networks (the number of input layer nodes is 2 and the number of hidden layer nodes is 3/4/5/6/7/8/9/10/11/12).

5) Empirical Line Method: The empirical linear radiometric correction method is to establish the linear regression relationship between the DN value and the SR, and solve its linear gain and bias coefficient. We used the real reflectance data from reflective boards to establish the linear relationship between DN value and reflectance of images with different bands, and realized the conversion from DN value to SR:

$$\text{Reflectance} = m \times DN + c \tag{6}$$

where m is the gain value and c represents the bias value.

We used goodness of fit (R^2) and root mean square error (RMSE) to evaluate the accuracy of ELM's regression fitting

$$R^2 = \frac{\sum_{i=1}^{n} (\hat{y}_i - \bar{y})^2}{\sum_{i=1}^{n} (y_i - \bar{y})^2} \tag{7}$$

$$\text{RMSE} = \sqrt{\frac{\sum_{i=1}^{n} (y_i - \hat{y}_i)^2}{n}} \tag{8}$$

where y and $\hat{y}$ denote sample point values (values to be fitted) and fitted values by ELM, respectively. $\bar{y}$ represents the mean value of y. n is the total number of sample points. The closer R^2 is to 1 and the smaller RMSE is, indicating that ELM's estimation of SR is more reliable.

6) Simplified Surface Reflectance Inversion Method Based on 6S Radiative Transfer Model: The flight altitude of UAV is generally low from the ground, the acquired image is little affected by atmospheric factors. Therefore, a simplified 6S RT model without considering atmospheric parameters can be used for radiometric correction of UAV remote sensing images.

Bilal et al. [52] developed an SR retrievals method [simplified and robust SR estimation method (SREM), is expressed as (9)–(17)] based on the 6S RT model. A series of experiments showed that SREM can be applied to multispectral remote sensing data of diverse land cover types acquired by different sensors

$$\rho_s = \frac{\rho_{IA} - \rho_R}{(\rho_{IA} - \rho_R) S_{\text{atm}} + T_s T_v} \tag{9}$$

where ρ_s is SR estimated by SREM, ρ_{IA} is reflectance received by UAV sensor in the atmosphere, ρ_R is atmospheric reflectance after Rayleigh scattering, S_{atm} represents atmospheric backscattering ratio to count multiple reflections between the surface and atmosphere. T_s and T_v are, respectively, the atmospheric downward and upward transmittance.

In (9), reflectance in the atmosphere (ρ_{IA}) is calculated using (10), and Rayleigh reflectance (ρ_R) is computed using (11)

$$\rho_{IA} = \frac{\pi L_{IA} d^2}{\text{ESUN}_\lambda \mu_s} \tag{10}$$

$$\rho_R = \frac{P_R \left(1 - e^{-M\tau_r}\right)}{4 (\mu_s + \mu_v)} \tag{11}$$

where L_{IA} is the radiance received by UAV sensor in the atmosphere, d is the distance (astronomical unit) between Sun and the Earth, ESUN is mean solar exoatmospheric irradiance (unit: $\mathrm{W}\cdot\mathrm{m}^{-2}\cdot\mu\mathrm{m}^{-1}$), λ is wavelength. In this article, the value of d is set to 1.014. The ESUN values of blue, green, red, red-edge and near infrared bands are 1930.9, 1854.8, 1556.5, 1356.7, and 1156.9, respectively. For (11), M is air mass calculated using (12), τ_r is Rayleigh optical depth calculated using (13), μ_s is cosine of solar zenith angle (SZA), and μ_v is cosine of sensor zenith angle, which is 0 owing to sensor getting the images vertically. In astronomy, the SZA and the SAA are complementary angles. We obtained the SZA by simple calculation (90°-SAA)

$$M = \frac{1}{\mu_s} + \frac{1}{\mu_v} \tag{12}$$

$$\tau_r = 0.008569\frac{1}{\lambda^4}\left(1 + 0.0113\frac{1}{\lambda^2} + 0.00013\frac{1}{\lambda^4}\right) \tag{13}$$

$$P_R = \frac{3A}{4+B}\left(1+\cos^2\Theta\right) \tag{14}$$

where A and B in (14) are 0.9587256 and 0.0412744, respectively. Θ in (14) stands for scattering angle, which is gotten through the operation of SZA (180°-SZA) because of sensor vertical to ground.

In (9), the atmospheric backscattering ratio (S_{atm}) and total atmospheric transmission (T_sT_v) can be expressed as

$$S_{\mathrm{atm}} = (0.92\tau_r)\ e^{-\tau_r} \tag{15}$$

$$T_s\ (\lambda) = e^{(-\tau_r/\mu_s)} + e^{(-\tau_r/\mu_s)}\left\{e^{(0.52\tau_r/\mu_s)} - 1\right\} \tag{16}$$

$$T_v\ (\lambda) = e^{(-\tau_r/\mu_v)} + e^{(-\tau_r/\mu_v)}\left\{e^{(0.52\tau_r/\mu_v)} - 1\right\}. \tag{17}$$

7) Validation of Proposed Radiometric Correction Model: The evaluation of radiometric correction accuracy is performed in two ways. The first method is based on reflective boards with known reflectance in image. We compared the real reflectance with SR of each reflective board obtained through the BPNNRCM. Another method is to compare the results of the BPNNRCM with the classical radiometric correction method such as ELM model and 6S radiative transfer model. The radiometric correction accuracy can be quantified by standard deviation (SD), MSE, mean absolute error (MAE), and mean relative error (MRE)

$$\mathrm{SD} = \sqrt{\frac{\sum_{i=1}^{m}\left(\mathrm{SR}_{\mathrm{calculated},i} - \overline{\mathrm{SR}}_{\mathrm{calculated}}\right)^2}{m-1}} \tag{18}$$

$$\mathrm{MSE} = \frac{1}{m}\sum_{i=1}^{m}\left(\mathrm{SR}_{\mathrm{calculated},i} - \mathrm{SR}_{\mathrm{real/ELM/6}S,i}\right)^2 \tag{19}$$

$$\mathrm{MAE} = \frac{1}{m}\sum_{i=1}^{m}\left|\mathrm{SR}_{\mathrm{calculated},i} - \mathrm{SR}_{\mathrm{real/ELM/6}S,i}\right| \tag{20}$$

$$\mathrm{MRE} = \frac{100\%}{m}\sum_{i=1}^{m}\frac{\left|\mathrm{SR}_{\mathrm{calculated},i} - \mathrm{SR}_{\mathrm{real/ELM/6}S,i}\right|}{\mathrm{SR}_{\mathrm{real/ELM/6}S,i}} \tag{21}$$

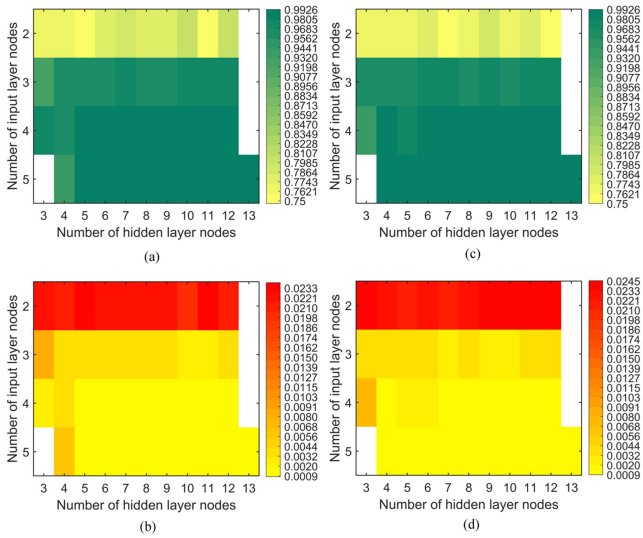

Fig. 5. Accuracy of BP neural network constructed by different parameters (number of nodes in input layer and hidden layer). (a) R of validation dataset. (b) MSE of validation dataset. (c) R of test dataset and (d) MSE of test dataset.

where $\mathrm{SR}_{\mathrm{calculated}}$ is the SR calculated by the BPNNRCM proposed in this article, $\overline{\mathrm{SR}}_{\mathrm{calculated}}$ is the average value of $\mathrm{SR}_{\mathrm{calculated}}$, $\mathrm{SR}_{\mathrm{real/ELM/6S}}$ is the SR which is gotten from reflective boards (with known real reflectance)/ELM model/6S model, and m is the total number of samples.

Moreover, MSE (19) and regression R value (22) refer the radiometric correction effect of BP neural network constructed with different parameters in validation set and test set

$$R = \frac{\mathrm{Cov}\left(\mathrm{SR}_{\mathrm{calculated}}, \mathrm{SR}_{\mathrm{real}}\right)}{\sqrt{\mathrm{Var}\left[\mathrm{SR}_{\mathrm{calculated}}\right]\mathrm{Var}\left[\mathrm{SR}_{\mathrm{real}}\right]}} \tag{22}$$

where $\mathrm{Cov}(\mathrm{SR}_{\mathrm{calculated}},\mathrm{SR}_{\mathrm{real}})$ denotes the covariance of $\mathrm{SR}_{\mathrm{calculated}}$ and $\mathrm{SR}_{\mathrm{real}}$, $\mathrm{Var}[\mathrm{SR}_{\mathrm{calculated}}/\mathrm{SR}_{\mathrm{real}}]$ is the variance of $\mathrm{SR}_{\mathrm{calculated}}/\mathrm{SR}_{\mathrm{real}}$. MSE represents the average squared difference between outputs ($\mathrm{SR}_{\mathrm{calculated}}$) and targets ($\mathrm{SR}_{\mathrm{real}}$). Lower values were better. Zero meant no error. Regression R value measured the correlation between outputs and targets. An R value of 1 meant a close relationship, 0 a random relationship.

III. Results

A. Determination of Optimal Parameters of BP Neural Network for Radiometric Correction

A total of 5180 sample points were collected by taking the mean DN value of the three neighborhoods in the center of the reflective boards as the DN value of the corresponding image. The reflectances of the reflective boards are known, and they are directly taken as the true value (output data of neural network model) of the sample point. Training sample points, validation sample points and testing sample points were randomly selected according to the proportion of 70%, 15% and 15% respectively.

We tested the effect of the BP neural network model constructed with different input parameters of each combination in Table III. Fig. 5 reveals the MSE and regression R value of BP

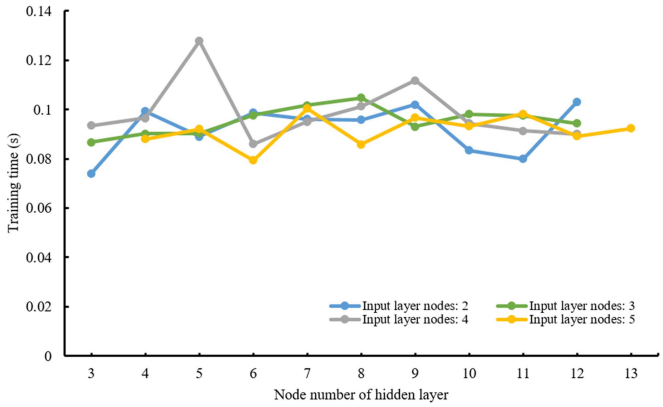

Fig. 6. Training time of BP neural network constructed by different parameters with different numbers of input layer and hidden layer nodes.

neural network constructed with different parameters in validation and testing dataset. BP neural network with different parameters had different MSE and *R* values. Fig. 6 shows the training time of neural networks composed of various input/hidden layer nodes. The number of training samples corresponding to the training time was 3626, accounting for 70% of the 5180 samples mentioned above. The training time of BP neural network varied with the number of nodes in input layer and hidden layer. In the range of the number of input/hidden layer nodes involved in this article, the training time was between 0.0741 and 0.1277 seconds. BP neural network with different parameters had different MSE and R values. The *R* value varied from 0.75 to 0.99. The MSE value ranged from 0.0009 to 0.0245. When the number of nodes in the input layer was 2, the error of the model was generally large both in validation and test dataset, and the maximum MSE value was 0.0245. When the number of nodes in the input layer was greater than 3 and the number of nodes in the hidden layer was greater than 6, the accuracy of BP neural network model was generally high (*R* values were above 0.98 and MSE were below 0.002). Considering the training accuracy and training time of BP neural network model with different parameters, when the *R* value was greater than 0.98 and the MSE value was less than 0.002, the shortest training time was 0.0858 seconds, hence the optimal parameters of the BP neural network radiometric correction model were: the number of nodes in the input layer was 5 (combination 4 in Table III), the number of nodes in the hidden layer was 8.

B. Accuracy Verification of Model With Optimal Parameters

1) Comparing SR Obtained by the BPNNRCM With Real Reflectance of Reflective Boards: The BP neural network model with optimal parameters obtained in Section III-A was used for radiometric correction of UAV multispectral images (see Table IV shows UAV multispectral images information). The reflectance of the reflective boards obtained by BPNNRCM was compared with the real reflectance of the reflective boards, so as to verify the accuracy of the BPNNRCM. Fig. 7 represents the SR products gotten by radiometric correction model based

TABLE IV
UAV MULTISPECTRAL IMAGES TO VERIFY ACCURACY OF BPNNRCM

Image	Band (nm)	Image Height (m)	SAA (°)
1	450	40	68.21
2	550	160	42.74
3	650	280	74.13
4	725	320	61.96
5	850	440	68.21
6	450	60	79.22
7	550	140	68.25
8	650	260	79.22
9	725	340	68.25
10	850	460	79.22

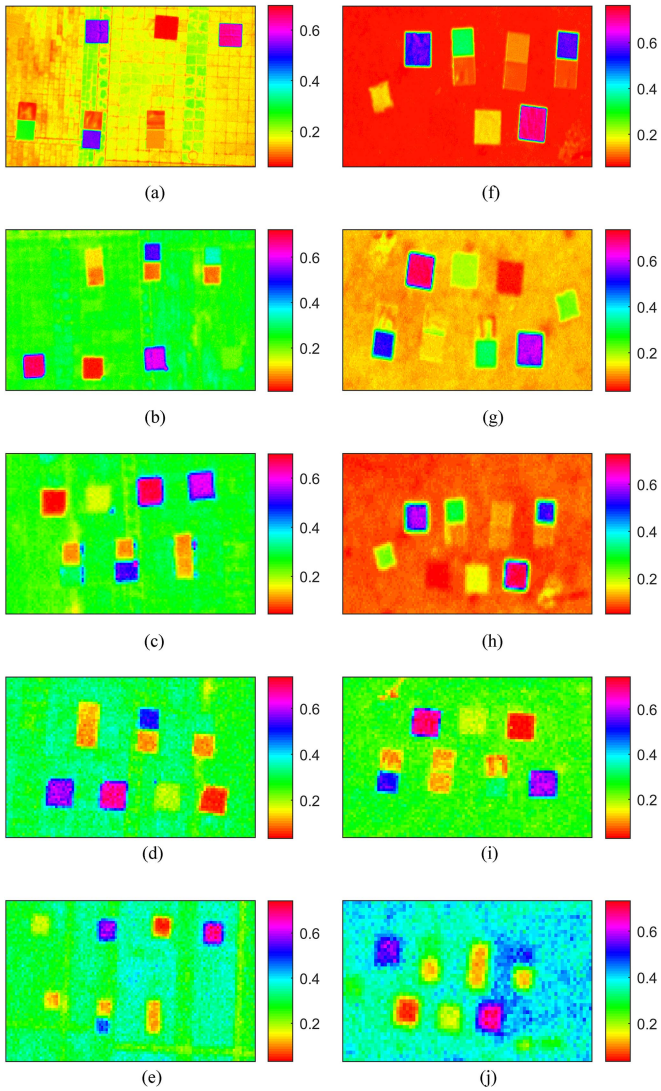

Fig. 7. SR obtained based on the BPNNRCM, where (a)–(j) correspond to images 1 ∼ 10 in Table IV.

TABLE V
REFLECTANCE OF EACH REFLECTIVE BOARD IN TEN IMAGES (SEE TABLE IV FOR IMAGE INFORMATION) CALCULATED BY BPNNRCM

	True Reflectance of Reflective Boards						
	0.05	**0.1**	**0.2**	**0.3**	**0.5**	**0.6**	**0.7**
Image 1	0.0616	0.1206	0.1798	0.2827	0.5192	0.5741	0.6707
Image 2	0.0475	0.1132	0.1956	0.3239	0.5246	0.6045	0.6846
Image 3	0.0514	0.1234	0.1777	0.302	0.5134	0.5851	0.6879
Image 4	0.0521	0.1202	0.206	0.3028	0.5126	0.5921	0.6899
Image 5	0.0402	0.1038	0.1977	0.2856	0.5247	0.5975	0.7264
Image 6	0.0677	0.1196	0.1702	0.3213	0.5535	0.6001	0.7127
Image 7	0.051	0.1301	0.1977	0.3062	0.5138	0.594	0.7145
Image 8	0.0515	0.1212	0.1774	0.2966	0.5225	0.5948	0.7159
Image 9	0.0466	0.1122	0.1806	0.3117	0.5254	0.6161	0.723
Image 10	0.0596	0.1208	0.1948	0.3122	0.4926	0.5721	0.701
Maximum error	0.0177	0.0301	0.0298	0.0239	0.0535	0.0279	0.0293
Minimum error	0.001	0.0038	0.0023	0.002	0.0074	0.0001	0.001
Standard deviation	0.008	0.0072	0.0119	0.0136	0.0152	0.0133	0.0186
MSE ($\times 10^{-4}$)	0.6635	3.8897	2.7735	1.8791	6.1811	2.0824	3.1954
MAE	0.0061	0.0185	0.0135	0.0115	0.0217	0.0111	0.016
MRE (%)	12.12	18.51	6.73	3.84	4.34	1.85	2.29

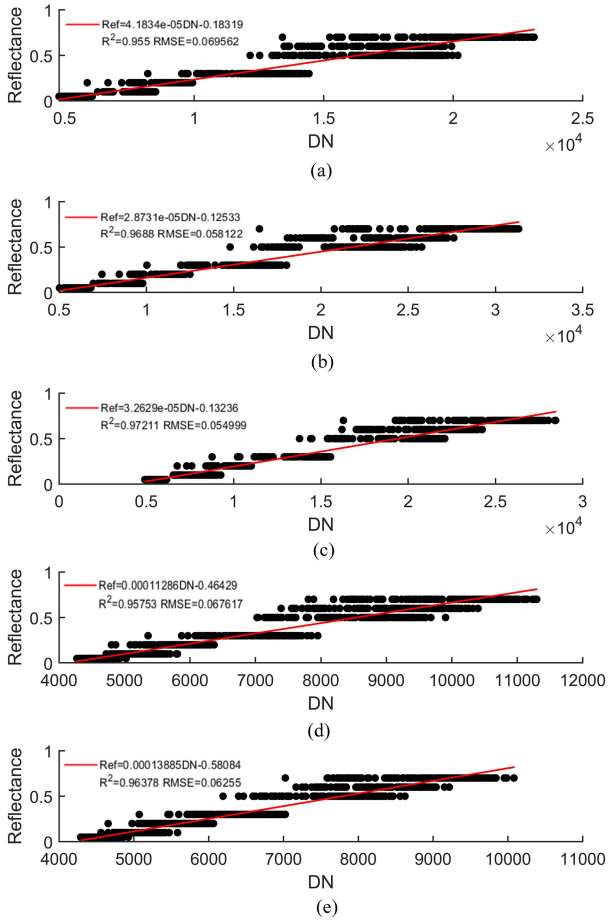

Fig. 8. ELM radiometric correction model for different bands. (a) 450 nm. (b) 550 nm. (c) 650 nm. (d) 725 nm. (e) 850 nm.

on BP neural network with optimal parameters proposed in this article. A total of 7 reflective boards with different reflectance (0.05, 0.1, 0.2, 0.3, 0.5, 0.6 and 0.7) were evenly distributed in each image. The spatial position of each reflective board could be clearly seen through SR results of Fig. 7, and the SR distribution of different ground objects (brick floor and grassland) could also be obtained.

The central pixel value of each reflective board in each radiation-corrected image (the average value of 3 × 3 neighborhood) was collected and counted. The reflectance of each reflective board in ten scene images after radiometric correction based on the BPNNRCM are displayed in Table V. Table V gives the maximum error, minimum error, SD, MSE, MAE and MRE calculated based on the SR obtained through the proposed radiometric correction model (BPNNRCM) in this article. The maximum/minimum error represented the maximum/minimum absolute value of the difference between the reflectance of the reflective board obtained by BPNNRCM and the true reflectance of the reflective board. In all ten images, each reflective board's reflectance error was not greater than 0.0535. The mean values of SD, MSE, MAE and MRE of all reflective boards obtained by BPNNRCM were 0.0125, 2.9521×10^{-4}, 0.0141 and 7.1%, respectively, in the images of different wavelength, height, date and time.

2) Comparing the Radiometric Correction Performance of BPNNRCM With ELM and SREM: Based on the 5180 sample points mentioned in Section III-A (each sample point had DN value and corresponding reflectance value), radiometric correction model of different bands based on ELM were constructed, and the model construction results are shown in Fig. 8. "Ref" in the legend indicated reflectance. Fig. 8 shows the gain and bias coefficients of the empirical linear model for each band, as well as the R^2 and RMSE of the model for sample points. For the five bands, R^2 were all above 0.95 and RMSE were all less than 0.07. With the increase of wavelength, the gain value showed an increasing trend. The gain value of green band was the smallest, which was 2.8731×10^{-5}. The gain value of near infrared band was the largest, which was 1.3885×10^{-4}. The bias values were all less than zero and ranged from −0.58084 to −0.12533.

SR products gotten based on ELM and SREM are revealed in Figs. 9 and 10, respectively. The image information (see Table IV) and reflectance of each reflective board were consistent with those in Section III-B-a. The central pixel value of each reflective board in each radiation-corrected image (the average value of 3 × 3 neighborhood) was collected and counted. The reflectance of each reflective board in ten scene images after

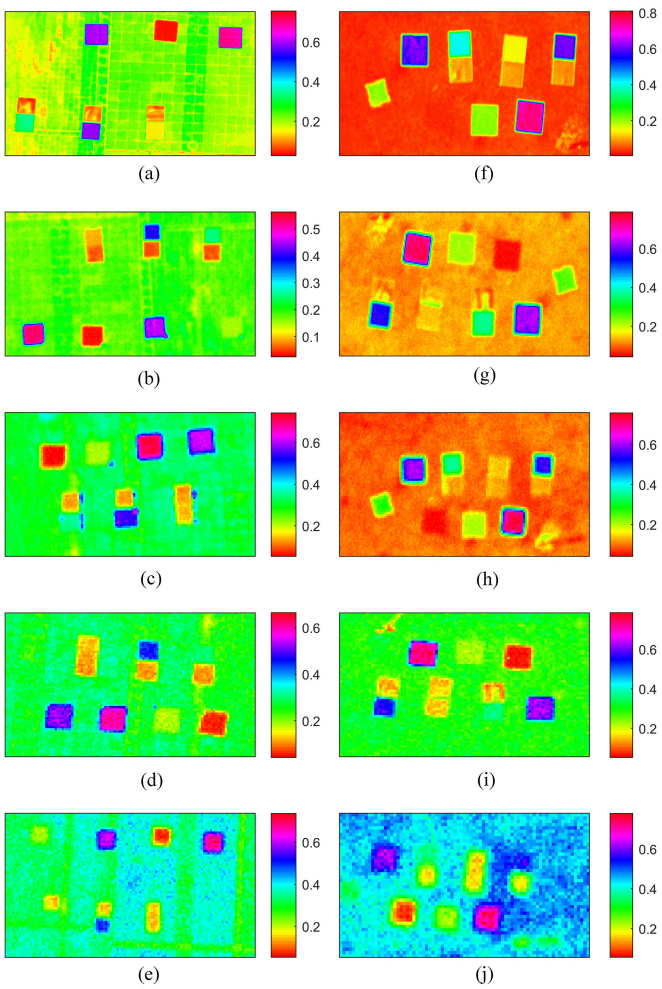

Fig. 9. SR obtained based on the ELM method, where (a)–(j) correspond to images 1–10 in Table IV.

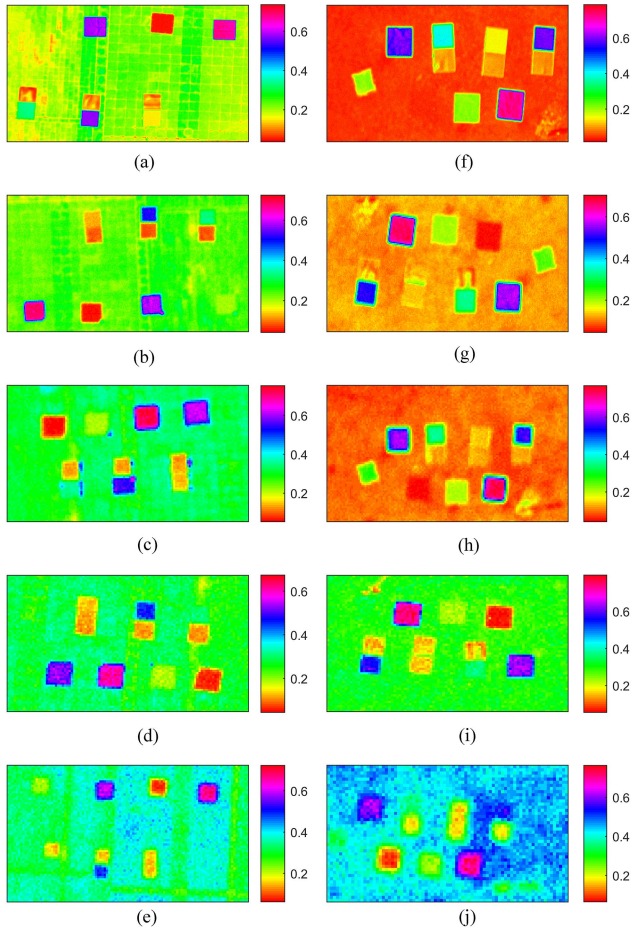

Fig. 10. SR obtained based on the SREM method, where (a)–(j) correspond to images 1–10 in Table IV.

radiometric correction based on ELM and SREM are respectively displayed in Tables VI and VII.

Table VI gives the maximum error, minimum error, SD, MSE, MAE, and MRE calculated based on the SR obtained through the ELM. In all ten images, the absolute errors of reflectance of reflective boards ranged from 0.0019 to 0.1721. The average absolute error of ELM was 0.0351. The mean values of SD, MSE, MAE and MRE of all reflective boards obtained by ELM were 0.0383, 0.0021, 0.0351 and 14.88%, respectively, in the images of different wavelength, height, date and time.

Table VII gives the maximum error, minimum error, SD, MSE, MAE and MRE calculated based on the SR obtained through the SREM. In all ten images, the absolute errors of reflectance of reflective boards ranged from 0.001 to 0.0846. The average absolute error of SREM was 0.0267. The mean values of SD, MSE, MAE, and MRE of all reflective boards obtained by SREM were 0.0201, 0.001, 0.0267 and 12.62%, respectively, in the images of different wavelength, height, date and time.

The accuracy of radiometric correction results varied with different methods. Fig. 11 shows the average SD, MSE, MAE, and MRE of SR retrieved by different methods. The values of

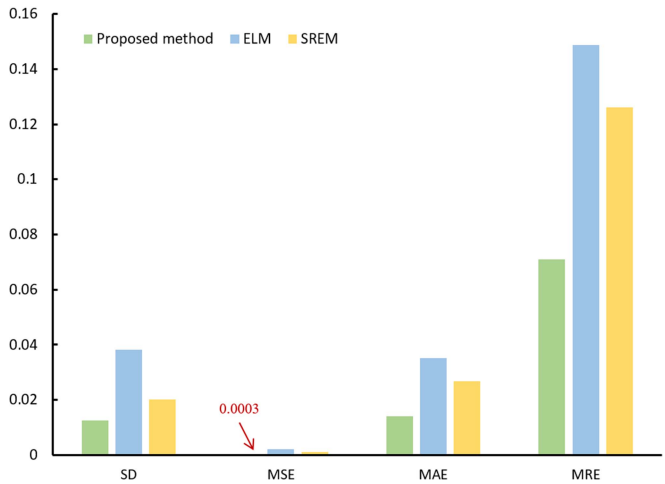

Fig. 11. Comparison of accuracy of three radiometric correction methods: BPNNRCM; ELM; and SREM.

MSE were generally small, with a minimum value of 0.0003. On the whole, the SD, MSE, MAE and MRE of the ELM method were relatively large. Compared with the ELM and SREM (simplified 6S RT model), the SR obtained by BPNNRCM had higher accuracy.

TABLE VI
REFLECTANCE OF EACH REFLECTIVE BOARD IN TEN IMAGES (SEE TABLE IV FOR IMAGE INFORMATION) CALCULATED BY ELM

	True Reflectance of Reflective Boards						
	0.05	**0.1**	**0.2**	**0.3**	**0.5**	**0.6**	**0.7**
Image 1	0.035	0.1475	0.1655	0.3175	0.5772	0.5825	0.6602
Image 2	0.0328	0.0939	0.1477	0.2645	0.4052	0.4658	0.5279
Image 3	0.0608	0.1339	0.2148	0.3589	0.5312	0.6267	0.727
Image 4	0.0558	0.1316	0.1876	0.3104	0.4603	0.5361	0.6137
Image 5	0.0657	0.1301	0.2345	0.3189	0.5477	0.6299	0.7232
Image 6	0.037	0.1334	0.2157	0.3884	0.5999	0.5966	0.7412
Image 7	0.048	0.1316	0.2213	0.3454	0.5546	0.6322	0.7315
Image 8	0.0519	0.1355	0.2122	0.3318	0.5406	0.6079	0.7217
Image 9	0.0648	0.137	0.2075	0.3501	0.5343	0.6101	0.7311
Image 10	0.0723	0.1367	0.2145	0.3478	0.5077	0.5877	0.7477
Maximum error	0.0223	0.0475	0.0523	0.0884	0.0999	0.1342	0.1721
Minimum error	0.0019	0.0061	0.0075	0.0104	0.0077	0.0034	0.0217
Standard deviation	0.014	0.014	0.027	0.0334	0.0567	0.0514	0.0713
MSE	0.0002	0.0011	0.0007	0.0021	0.0036	0.0025	0.0046
MAE	0.0118	0.0323	0.022	0.0405	0.0528	0.0338	0.0522
MRE (%)	23.7	32.34	10.98	13.49	10.55	5.63	7.45

TABLE VII
REFLECTANCE OF EACH REFLECTIVE BOARD IN TEN IMAGES (SEE TABLE IV FOR IMAGE INFORMATION) CALCULATED BY SREM

	True Reflectance of Reflective Boards						
	0.05	**0.1**	**0.2**	**0.3**	**0.5**	**0.6**	**0.7**
Image 1	0.0488	0.1393	0.1702	0.3371	0.558	0.6261	0.6948
Image 2	0.0579	0.1217	0.1977	0.3275	0.5317	0.6258	0.6837
Image 3	0.0547	0.1375	0.2172	0.3547	0.539	0.6102	0.7158
Image 4	0.0585	0.1243	0.1901	0.3162	0.4953	0.5502	0.6562
Image 5	0.0622	0.135	0.2272	0.3365	0.4908	0.5787	0.7095
Image 6	0.0424	0.1419	0.2183	0.3846	0.5702	0.6074	0.7371
Image 7	0.0566	0.1392	0.2026	0.3239	0.4936	0.5656	0.6762
Image 8	0.051	0.1328	0.1975	0.3526	0.5581	0.6325	0.744
Image 9	0.0676	0.1444	0.212	0.3528	0.541	0.6489	0.7238
Image 10	0.0643	0.1372	0.2251	0.3472	0.5316	0.6237	0.7052
Maximum error	0.0176	0.0444	0.0298	0.0846	0.0702	0.0498	0.044
Minimum error	0.001	0.0217	0.0023	0.0162	0.0047	0.0074	0.0052
Standard deviation	0.0076	0.0073	0.0177	0.0196	0.0288	0.0319	0.0275
MSE	0.0001	0.0013	0.0003	0.0022	0.0017	0.001	0.0007
MAE	0.0082	0.0353	0.0147	0.0433	0.035	0.028	0.0225
MRE (%)	16.31	35.33	7.35	14.44	7	4.67	3.21

Overall, through the comparison with the results of classical radiometric correction model, the BPNNRCM had high accuracy in SR estimation and could meet the requirements of UAV multispectral image radiometric correction processing.

C. Robustness and Generalization of the BPNNRCM

In order to verify the universality, stability and generalization of the BPNNRCM, we used the BP neural network model with optimal parameters (input variables: DN value, UAV sensor height, wavelength, SAA and temperature; hidden layer nodes number: 8) trained in Section III-A to perform radiometric correction on the multispectral images collected by another UAV (FEIMA D2000 with D-MSPC2000 sensor), and cross-verify the validity of the BPNNRCM.

The radiometrically corrected results of BPNNRCM are shown in Fig. 12. UAV multispectral images 1–2 in Table II correspond to (a) and (b) in Fig. 12 respectively. The central pixel value of each reflective board in each radiation-corrected image (the average value of 3×3 neighborhood) was calculated. The reflectance of each reflective board in different images after model correction was obtained (see Table VIII). Table VIII gives the SD, MSE, MAE and MRE calculated based on the SR obtained through the BPNNRCM. The absolute errors of SR of reflective boards ranged from 0.0021 to 0.0451. The mean values of SD, MSE, MAE and MRE of all reflective boards were 0.0104, 0.0006, 0.0218, and 10.49%, respectively, which indicated that the proposed radiometric correction model (BPNNRCM) had good robustness and generalization.

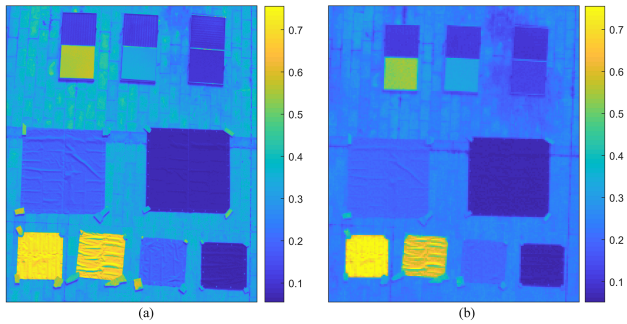

Fig. 12. Radiometrically corrected results of (a) image 1 and (b) image 2 in Table II.

IV. DISCUSSION

A. Performance Evaluation of Different Radiometric Correction Methods in Different Bands

We studied the radiometric correction accuracy of different wavelengths for the BPNNRCM, SREM based on 6S RT model and ELM. Fig. 13 shows the absolute errors between SR obtained by radiometric correction methods and the true reflectance of the reflective boards in images with different bands (see Table IV).

TABLE VIII
REFLECTANCE OF EACH REFLECTIVE BOARD IN DIFFERENT IMAGES (SEE TABLE II FOR IMAGE INFORMATION) CALCULATED BY BPNNRCM

	True Reflectance of Reflective Boards						
	0.05	**0.1**	**0.2**	**0.3**	**0.5**	**0.6**	**0.7**
Image 1	0.0687	0.0979	0.1882	0.3314	0.5451	0.6388	0.7306
Image 2	0.061	0.1276	0.1901	0.3171	0.5293	0.6171	0.7147
Maximum error	0.0187	0.0276	0.0118	0.0314	0.0451	0.0388	0.0306
Minimum error	0.011	0.0021	0.0099	0.0171	0.0293	0.0171	0.0147
Standard deviation	0.0054	0.018	0.0013	0.0101	0.0112	0.0153	0.0112
MSE	0.0002	0.0004	0.0001	0.0006	0.0014	0.0009	0.0006
MAE	0.0148	0.0148	0.0109	0.0242	0.0372	0.028	0.0227
MRE (%)	29.7	14.85	5.43	8.08	7.44	4.66	3.24

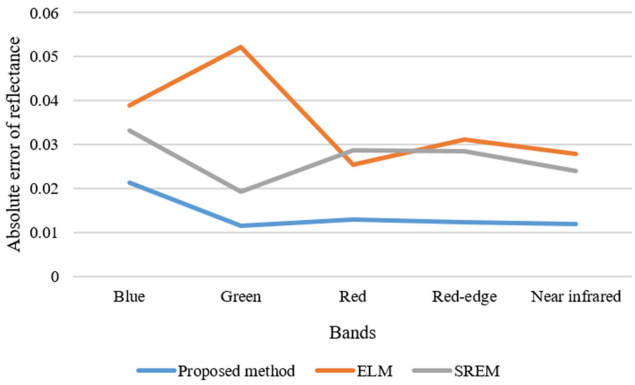

Fig. 13. Performance of three radiometric correction methods in different bands.

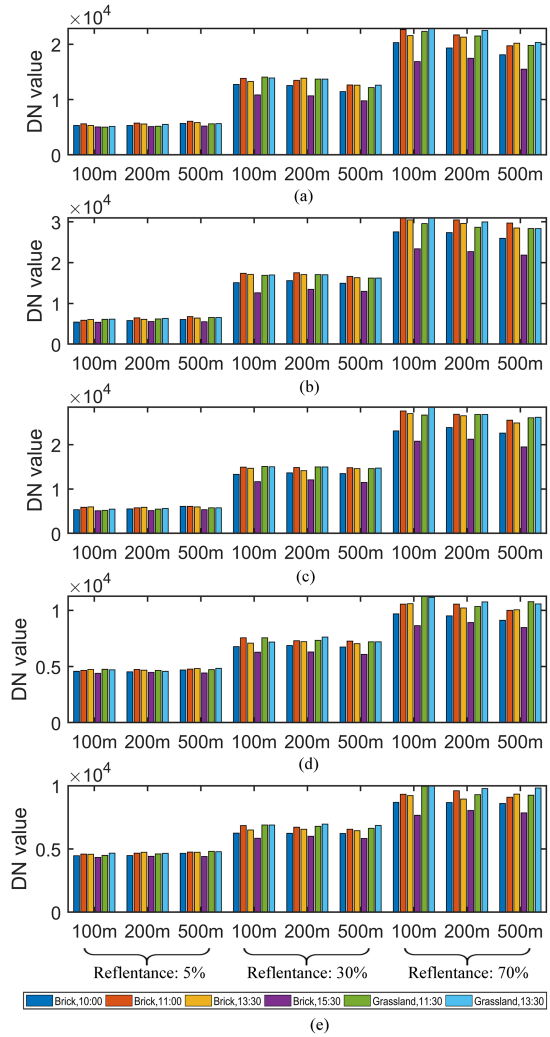

Fig. 14. DN values of reflective boards in different flight conditions and scenes. (a) 450 nm. (b) 550 nm. (c) 650 nm. (d) 725 nm. (e) 850 nm.

The absolute error of reflectance in red, red-edge and near infrared bands obtained by the same method was roughly the same. The average errors of ELM, SREM and BPNNRCM in the above three bands were 0.0281, 0.027, and 0.0124, respectively. The absolute error of blue band was greater than that of red, red-edge and near infrared bands. In the future, we will analyze the causes of the above phenomena and propose the improved radiometric correction methods for different bands.

B. Sensitivity of BPNNRCM to Ambient/Background Light

We analyzed the changes of DN values of reflective boards in different images (with different time, different image height, different wavelength and different ambient/background light) obtained by K6 sensor in Section II-A. It can be seen from Fig. 14 that the DN value increased with the increase of reflective boards' reflectance. The DN value of reflective board with high reflectance (70%) showed a decreasing trend with the increase of image height. With the same SAA, image height and wavelength, the DN values of the same reflective board in different ambient/background light was roughly the same, and there was no significant difference. The main factors for the difference of DN values of reflective boards in the images were the time of image acquisition (SAA), height and wavelength. Ambient/background light had little effect on the DN value obtained by the radiation of the target (reflective boards) received through the UAV sensor.

TABLE IX
UAV MULTISPECTRAL IMAGES WITH DIFFERENT AMBIENT/BACKGROUND LIGHT

Image	**Wavelength (nm)**	**Image Height (m)**	**SAA (°)**	**Ambient/ Background**
1	550	140	68.2	Brick
2	550	140	68.2	Grassland

Furthermore, we used BPNNRCM model to conduct radiometric correction for the images of conditions 3 and 6 in Table I, and the image information is given in Table IX. We ensured the consistency of image height, image wavelength and SAA, so as to study the affect of ambient/background light on the

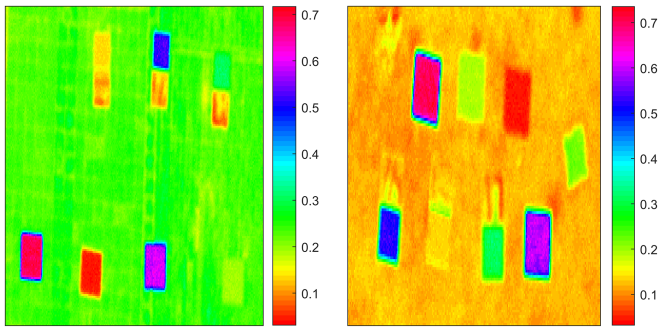

Fig. 15. Radiometrically corrected results of images with distinct ambient/background light. (a) Brick and (b) grassland.

TABLE X
REFLECTANCE OF EACH REFLECTIVE BOARD IN IMAGES WITH DIFFERENT AMBIENT/BACKGROUND LIGHT CALCULATED BY BPNNRCM (SEE TABLE IX FOR IMAGE INFORMATION)

	True Reflectance of Reflective Boards						
	0.05	**0.1**	**0.2**	**0.3**	**0.5**	**0.6**	**0.7**
Image 1	0.0461	0.1325	0.1935	0.3063	0.5053	0.602	0.6946
Image 2	0.0459	0.1324	0.194	0.3071	0.5077	0.601	0.6944
Error between two images	0.0002	0.0001	0.0005	0.0008	0.0024	0.001	0.0002

radiometric correction accuracy of BPNNRCM. The SR of the two images in Table IX obtained by BPNNRCM is shown in Fig. 15. The reflectance of each reflective board in different images after BPNNRCM correction was obtained (see Table X). Moreover, Table X gives the absolute error of the same reflective board's SR in different ambient/background light obtained by BPNNRCM. The absolute errors of SR of same reflective board ranged from 0.0001 to 0.0024. The errors were very small, which indicated that ambient/background light had little effect on the accuracy of BPNNRCM model.

C. More Versatility Method for Radiometric Correction of UAV Multispectral Image

Cao et al. [53] improved the performance of three UAV remote sensing reflectance obtention methods (MIR, ELM, and ARTM) based on incident, background and environmental radiance. The average absolute error of MIR, ELM, and ARTM were 0.018, 0.017, and 0.044, respectively. The average absolute error of the BPNNRCM in this article was 0.0141. The average absolute error of SR acquisition by BPNNRCM was less than that by improved MIR, ELM, and ARTM. However, for our experimental data, the UAV sensor acquired the image at a shooting angle of 90°, that is, perpendicular to the ground. The DN value of UAV sensor is closely related to the angle between its sensor and ground object, and the regular between DN value change and angle change needs to be explored. At the same time, it is of great significance to construct a novel radiometric correction model for UAV remote sensing suitable for different observation angles. At present, the BPNNRCM proposed in this article only applies to the multispectral data of common bands (blue band, green band, red band, red-edge band, and near infrared band). We will verify the feasibility and universality of the BPNNRCM for radiometric correction of hyperspectral and thermal infrared data in the future. In addition, the UAV multispectral image data in this article were all collected in relatively flat areas. In the future, we will try to collect UAV multispectral data in mountainous areas, considering the impact of terrain effect on radiometric correction, so as to further increase the versatility of the BPNNRCM proposed in this article.

V. CONCLUSION

This article proposed a BPNNRCM taking into account optimal parameters. The different combinations of input variables and hidden layer nodes number constituted multiple BP neural networks with different parameters. We comprehensively considered the MSE and R values of different BP neural networks in the validation and test set, as well as the training time of different BP neural networks, and finally determined the optimal parameters of BP neural network suitable for UAV multispectral image radiometric correction: the input variables were DN value, UAV sensor height, wavelength, SAA and temperature; the number of nodes in the hidden layer was 8, and its MSE and R were 0.00098/0.001 and 0.9911/0.9901 in validation/test dataset, respectively. We verified the accuracy and robustness of radiometric correction model based on BP neural network considering the optimal parameters. In the aspect of accuracy, we compared SR obtained by the BPNNRCM with reflective boards' real reflectance, ELM and 6S RT model. The absolute error of SR inversion obtained by the BPNNRCM was less than 0.054. The average absolute error of SR inversion obtained by the BPNNRCM was 0.0141. Compared with ELM and SREM (simplified 6S model), the BPNNRCM had smaller mean MSE (0.0003), MAE (0.0141) and MRE (7.1%). In the aspect of the robustness and generalization of the BPNNRCM, the trained BP neural network model was used for radiometric correction of multispectral images of different UAV, different sensors, different heights, different locations and different SAAs. The absolute errors of reflectance were all within 0.0451. The BPNNRCM for UAV multispectral image showed good performance in accuracy and robustness. This proves that the BPNNRCM can calculate the SR of UAV multispectral image with high precision under different UAV flight conditions. The radiometric correction algorithm (BPNNRCM) based on BP neural network with the optimal parameters has a relatively strong potential.

ACKNOWLEDGMENT

The authors would like to thank the equipment and pilot support from Shenzhen DJI Innovation Technology Co., Ltd. and Shenzhen Pegasus Robot Technology Co., Ltd.

REFERENCES

[1] R. Zhou, Y. Ou, B. Yu, and Q. Wang, "Research of geomatric and radiation correction of the hyperspectral imaging system carried by a multirotor unmanned aerial vehicle," *J. Southwest Univ.*, vol. 41, no. 9, pp. 141–147, 2019.

[2] L. De Beer, *Unmanned Aircraft Systems (Drones) and Law*. Nijmegen, The Netherlands: Wolf Legal Publishers, 2011.

[3] B. Qin and L. Wang, "Overview of UAV development," *Aerodyn. Missile J.*, vol. 8, pp. 4–10, 2002.

[4] R. Schroer, "UAVs: The future. [A century of powered flight: 1903-2003]," *IEEE Aerosp. Electron. Syst. Mag.*, vol. 18, no. 7, pp. 61–63, Jul. 2003.

[5] Y. Lin, L. Zhu, and H. Wang, "Technical characteristics and application trend of global Eagle unmanned reconnaissance aircraft," *Aerodyn. Missile J.*, vol. 9, pp. 21–24, 2011.

[6] L. Yan et al., "The impact of UAV remote sensing technology on the industrial development of China: A review," *J. Geo-Inf. Sci.*, vol. 21, no. 4, pp. 476–495, 2019.

[7] M. Wehrhan, P. Rauneker, and M. Sommer, "UAV-Based estimation of carbon exports from heterogeneous soil Landscapes—A case study from the CarboZALF experimental area," *Sensors*, vol. 16, no. 2, 2016, Art. no. 255.

[8] M. Hassanalian and A. Abdelskefi, "Classifications, applications, and design challenges of drones: A review," *Prog. Aerosp. Sci.*, vol. 91, pp. 99–131, 2017.

[9] Q. Qin et al., "A discussion on some frontier directions of quantitative remote sensing," *Remote Sens. Natural Resour.*, vol. 32, no. 4, pp. 8–15, 2020.

[10] D. Yu, Z. Deng, F. Long, H. Guan, Y. Gou, and D. Wang, "An lmplementation of the model of atmosphere automatic rectification based on linear regression method," *J. Shenyang Ligong Univ.*, vol. 27, no. 6, pp. 35–39, 2008.

[11] C. Wang and S. W. Myint, "A simplified empirical line method of radiometric calibration for small unmanned aircraft systems-based remote sensing," *IEEE J. Sel. Topics Appl. Earth Observ. Remote Sens.*, vol. 8, no. 5, pp. 1876–1885, May 2015.

[12] J. Kelcey and A. Lucieer, "Sensor correction and radiometric calibration of a 6-Band multispectral imaging sensor for UAV remote sensing," *ISPRS - Int. Arch. Photogramm., Remote Sens. Spatial Inf. Sci.*, vol. 39-B1, no. 9, pp. 393–398, 2012.

[13] Y. Duan, L. Yan, B. Yang, X. Jing, and W. Chen, "Outdoor relative radiometric calibration method using gray scale targets," *Sci. China Technol. Sci.*, vol. 56, no. 7, pp. 1825–1834, 2013.

[14] A. Matese, S. F. Di Gennaro, and L. G. Santesteban, "Methods to compare the spatial variability of UAV-based spectral and geometric information with ground autocorrelated data. A case of study for precision viticulture," *Comput. Electron. Agriculture*, vol. 162, pp. 931–940, 2019.

[15] A. M. Poncet, T. Knappenberger, C. Brodbeck, M. Fogle, J. N. Shaw, and B. V. Ortiz, "Multispectral UAS data accuracy for different radiometric calibration methods," *Remote Sens.*, vol. 11, no. 16, pp. 2019, Art. no. 1917.

[16] H. Cao, X. Gu, X. Wei, T. Yu, and H. Zhang, "Lookup table approach for radiometric calibration of miniaturized multispectral camera mounted on an unmanned aerial vehicle," *Remote Sens.*, vol. 12, no. 24, 2020, Art. no. 4012.

[17] J. F. Burkhart et al., "Unmanned aerial system nadir reflectance and MODIS nadir BRDF-adjusted surface reflectances intercompared over Greenland," *Cryosphere*, vol. 11, no. 4, pp. 1575–1589, 2017.

[18] B. Mamaghani and C. Salvaggio, "Multispectral sensor calibration and characterization for sUAS remote sensing," *Sensors*, vol. 19, no. 20, 2019, Art. no. 4453.

[19] A. Burkart, S. Cogliati, A. Schickling, and U. Rascher, "A novel UAV - based ultra - light weight spectrometer for field spectroscopy," *IEEE Sensors J.*, vol. 14, no. 1, pp. 62–67, Jan. 2014.

[20] W. Fan, X. Sun, Y. Wang, and A. Yang, "Atmospheric correction of remote sensing data based on two radiative transfer models and contrast analysis of the results," *J. Northeast Univ.*, vol. 37, no. 7, pp. 121–124, 2009.

[21] W. Zheng and Z. Zeng, "A review on methods of atmospheric correction for remote sensing lmages," *Remote Sens. Inf.*, vol. 4, pp. 66–70, 2004.

[22] J. R. Schott, C. Salvaggio, and W. J. Volchok, "Radiometric scene normalization using pseudoinvariant features," *Remote Sens. Environ.*, vol. 26, no. 1, pp. 1–14, 1988.

[23] F. G. Hall, D. B. Botkin, D. E. Strebel, K. D. Woods, and S. J. Goetz, "Large-Scale patterns of forest succession as determined by remote sensing," *Ecology*, vol. 72, no. 2, pp. 628–640, 1991.

[24] P. S. C. Jr, "Image-based atmospheric corrections-Revisited and improved," *Eng. Remote Sens.*, vol. 62, no. 9, pp. 1025–1036, 1996.

[25] M. S. Moran, R. D. Jackson, P. N. Slater, and P. M. Teillet, "Evaluation of simplified procedures for retrieval of land surface reflectance factors from satellite sensor output," *Remote Sens. Environ.*, vol. 41, no. 2, pp. 169–184, 1992.

[26] M. A. Gilabert, C. Conese, and F. Maselli, "An atmospheric correction method for the automatic retrieval of surface reflectances from TM images," *Int. J. Remote Sens.*, vol. 15, no. 10, pp. 2065–2086, 1994.

[27] H. Jiang, N. Lv, and L. Yao, "HOT-transform based method to remove haze or thin cloud for Landsat 8 OLI satellite data," *J. Remote Sens.*, vol. 20, no. 4, pp. 620–631, 2016.

[28] Y. Zhang, B. Guindon, and J. Cihlar, "An image transform to characterize and compensate for spatial variations in thin cloud contamination of Landsat images," *Remote Sens. Environ.*, vol. 82, no. 2, pp. 173–187, 2002.

[29] S. Von Bueren, A. Burkard, A. Hueni, U. Rascher, M. Tuohy, and I. Yule, "Deploying four optical UAV-Based sensors over grassland: Challenges and limitations," *Biogeosciences*, vol. 12, pp. 163–175, 2015.

[30] W. Farrand, R. Singer, and E. Merényu, "Retrieval of apparent surface reflectance from AVIRIS data: A comparison of empirical line, radiative transfer, and spectral mixture methods," *Remote Sens. Environ.*, vol. 47, pp. 311–321, 1994.

[31] G. Smith and E. Milton, "The use of the empirical line method to calibrate remotely sensed data to reflectance," *Int. J. Remote Sens.*, vol. 20, pp. 2653–2662, 1999.

[32] R. G. Isaacs, W. C. Wang, R. D. Worsham, and S. Goldengerg, "Multiple scattering LOWTRAN and FASCODE models," *Appl. Opt.*, vol. 26, no. 7, pp. 1272–1281, 1987.

[33] A. Berk et al., "MODTRAN5: A reformulated atmospheric band model with auxiliary species and practical multiple scattering options," in *Proc. SPIE Multispectral Hyperspectral Remote Sens. Instrum. Appl. II*, 2004, pp. 341–347.

[34] E. F. Vermote, D. Tanre, J. L. Deuze, M. Herman, and J. J. Morcette, "Second simulation of the satellite signal in the solar spectrum, 6S: An overview," *IEEE Trans. Geosci. Remote Sens.*, vol. 35, no. 3, pp. 675–686, May 1997.

[35] C. Cheng, Y. Wei, Y. Li, and Q. Tu, "Atmospheric correction of GF-1/WFV image in taihu lake based on the 6S model pixel by pixel," *Remote Sens. Technol. Appl.*, vol. 35, no. 1, pp. 141–152, 2020.

[36] K. Tachiiri, "Calculating NDVl for NOAA/AVHRR data after atmospheric correction for extensive images using 6S code: A case study in the marsabit district, Kenya," *ISPRS J. Photogramm. Remote Sens.*, vol. 59, no. 3, pp. 103–114, 2005.

[37] T. Fuyi, S. K. Mohammed, K. Abdullah, H. S. Lim, and K. S. Ishola, "A comparison of atmospheric correction techniques for environmental applications," in *Proc. IEEE Int. Conf. Space Sci. Commun.*, 2013, pp. 233–237.

[38] S. R. Proud, R. Fensholt, M. O. Rasmussen, and I. Sandholt, "A comparison of the effectiveness of 6S and SMAC in correcting for atmospheric interference of meteosat second generation images," *J. Geophys. Res.-Atmos.*, vol. 115, no. D17, 2010, Art. no. D17209.

[39] X. Wen, G. Hu, and X. Yang, "Simulation experiments on adjacency effect of satellite remote sensing pixels," *J. Infrared, Millimeter, Terahertz Waves*, vol. 28, no. 1, pp. 46–49, 2009.

[40] M. W. Matthew et al., "Atmospheric correction of spectral imagery: Evaluation of the FLAASH algorithm with AVIRIS data," in *Proc. Appl. Imag. Pattern Recognit. Workshop*, 2002, pp. 157–163.

[41] J. Chen, C. He, and C. Yue, "Atmospheric correction of an advance land imager (ALl) image based on the FLAASH module," *J. Zhejiang A F Univ.*, vol. 28, no. 4, pp. 590–596, 2011.

[42] A. Berk et al., "MODTRAN cloud and multiple scattering upgrades with application to AVIRIS," *Remote Sens. Environ.*, vol. 65, no. 3, pp. 367–375, 1998.

[43] M. Nazeer, J. E. Nichol, and Y. K. Yung, "Evaluation of atmospheric correction models and Landsat surface reflectance product in an urban coastal environment," *Int. J. Remote Sens.*, vol. 35, pp. 6271–6291, 2014.

[44] H. Nguyen et al., "Optimal atmospheric correction for above-ground forest biomass estimation with the ETM+ remote sensor," *Sensors*, vol. 15, pp. 18865–18886, 2015.

[45] P. López-Serrano, J. Corral-Rivas, R. Díaz-Varela, J. Álvarez-González, and C. López-Sánchez, "Evaluation of radiometric and atmospheric correction algorithms for aboveground forest biomass estimation using Landsat 5 TM data," *Remote Sens.*, vol. 8, no. 5, 2016, Art. no. 369.

[46] S. Lolli, L. Alparone, A. Garzelli, and G. Vivone, "Haze correction for contrast-based multispectral pansharpening," *IEEE Geosci. Remote Sens. Lett.*, vol. 14, no. 12, pp. 2255–2259, Dec. 2017.

[47] G. Doxani et al., "Atmospheric correction inter-comparison exercise," *Remote Sens.*, vol. 10, no. 352, pp. 8493–8496, 2018.
[48] J. Wen, J. Zhao, S. Luo, and Z. Han, "The improvements of BP neural network learning algorithm," in *Proc. 5th Int. Conf. Signal Process.*, 2000, pp. 1647–1649.
[49] J. Li, J. Cheng, J. Shi, and F. Huang, "Brief introduction of back propagation (BP) neural network algorithm and its improvement," *Adv. Comput. Sci. Inf. Eng.*, vol. 169, pp. 553–558, 2012.
[50] L. Liu, J. Chen, and L. Xu, "Realization and application research of BP neural network based on MATLAB," in *Proc. Int. Seminar Future Biomed. Inf. Eng.*, 2008, pp. 130–133.
[51] A. N. Kolmogorov, "On the representation of continuous functions of many variables by superposition of continuous functions of one variable and addition," *Doklady Akademii Nauk SSSR*, vol. 114, no. 5, pp. 953–956, 1957.
[52] M. Bilal et al., "A simplified and robust surface reflectance estimation method (SREM) for use over diverse land surfaces using multi-sensor data," *Remote Sens.*, vol. 11, no. 11, 2019, Art. no. 1344.
[53] H. Cao, X. Gu, Y. Sun, H. Gao, Z. Tao, and S. Shi, "Comparing, validating and improving the performance of reflectance obtention method for UAV-Remote sensing," *Int. J. Appl. Earth Observ. Geoinf.*, vol. 102, 2021, Art. no. 102391.

Yin Zhang is currently working toward the M.S. degree in photogrammetry and remote sensing with the School of Remote Sensing and Information Engineering, Wuhan University, Wuhan, China.

His research interests include remote sensing image information extraction and UAV image radiometric correction.

Qingwu Hu received the Ph.D. degree in photogrammetry and remote sensing from Wuhan University, Wuhan, China, in 2007.

He is a Professor with the School of Remote Sensing and Information Engineering, Wuhan University. His research interests include 3S integrated mobile measurement, laser point cloud intelligent processing, laser vision fusion navigation and three-dimensional mapping, remote sensing archaeology and digital cultural heritage, and GIS engineering.

Hailong Li received the B.S. degree in electronic information science and technology from Shandong Normal University, Jinan, China, in 2014, and the M.S. degree in signal and information processing from Xidian University, Xian, China, in 2017.

He is currently with China Research Institute of Radiowave Propagation, Xinxiang, China. His research interests include atmospheric correction and image degradation.

Jiayuan Li received the Ph.D. degree in photogrammetry and remote sensing from Wuhan University, Wuhan, China, in 2018.

He is currently an Associate Researcher with the School of Remote Sensing and Information Engineering, Wuhan University. His research interests include photogrammetry, machine vision and remote sensing image processing.

Tiancheng Liu is currently working toward the M.S. degree in cartography and geography information system with the School of Remote Sensing and Information Engineering, Wuhan University, Wuhan, China.

His research interests include point cloud data processing and UAV image radiometric correction.

Yuting Chen is currently working toward the M.S. degree in photogrammetry and remote sensing with the School of Remote Sensing and Information Engineering, Wuhan University, Wuhan, China.

Her research interests include remote sensing image information extraction and UAV image radiometric correction.

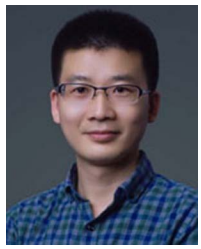

Mingyao Ai received the Ph.D. degree in photogrammetry and remote sensing from Wuhan University, Wuhan, China, in 2020.

He is currently working with the School of Remote Sensing and Information Engineering, Wuhan University. His research interests include three dimensional modeling and remote sensing image processing.

Jianye Dong received the B.S. degree in computer science and technology from Qingdao University of Technology, Qingdao, China, in 2005, and the M.S. degree in computer application technology from Shandong University of Science and Technology, Qingdao, China, in 2008.

He is currently with China Research Institute of Radiowave Propagation, Xinxiang, China. His research interests include atmospheric correction and thermal infrared remote sensing.